POLITECNICO MILANO 1863

SCUOLA DI INGEGNERIA INDUSTRIALE
E DELL'INFORMAZIONE

Executive Summary of the Thesis

Structural Modification and Experimental Correlation of an Aeroelastic Wind Tunnel Model for Flutter Analysis

Laurea Magistrale in Aeronautical Engineering – Ingegneria Aeronautica

Author: Teksen Atasoy

Advisor: PhD Francesco Toffol

Co-advisor: Prof. Sergio Ricci

Academic year: 2025–2026

Keywords

Aeroelastic wind-tunnel model; FEM updating; modal correlation; GVT;flutter analysis.

1. Introduction

Flutter assessment and aeroservoelastic studies rely on structural and aeroelastic models that are both predictive and consistent with the as-tested experimental configuration. In the context of the F-XDIA aeroelastic wind-tunnel demonstrator recent modifications of the support system and of the pylon to model interface introduced non-negligible changes in boundary conditions and low-frequency dynamics. These updates motivate a dedicated effort to revise the corresponding finite element model (FEM) and to re-establish a credible numerical representation of the current hardware.

The work presented in this thesis connects the evolving experimental set-up with its numerical counterpart by delivering an updated FEM correlated against Ground Vibration Test (GVT) data. Modal correlation is addressed through a physically motivated set of localized connection interface and pylon to model compliances represented by `CELAS` elements. Their values are updated via a constrained optimization loop implemented in MATLAB, and assessed by combined frequency agreement and mode-shape correlation metrics, with mode pairing validated through MAC matrices. A DMIG-based pathway is employed to integrate externally generated high-fidelity structural portions within the NeoCASS aeroservoelastic environment, preserving the dynamic contribution of critical substructures while maintaining a modular assembly.

Building on the correlated structural model,aeroelastic analyses are performed to compute flutter boundaries under the latest boundary-condition configurations. For the free-pitch installation (Configuration 3), the numerical prediction identifies a first instability at $V_{F,1} = 40.8$ m/s, in close agreement with the experimental FRF-based marker at $V \approx 40.2$ m/s. The associated flutter mechanism is interpreted as a symmetric bending–torsion coupling, and the comparison against wind-tunnel data is used to discuss model credibility, limitations, and possible extensions, including broader structural parameter updates and damping characterization .

2. F-XDIA model

2.1. Model overview

The F-XDIA is a scaled aeroservoelastic demonstrator designed for systematic flutter testing and for evaluating control-oriented methodologies, including AFS and the interaction between rigid-body stabilization (SAS). To enable repeatable testing while progressively increasing experimental realism, the installation method evolved through four representative boundary-condition configurations, spanning a baseline clamped support and released pitch/roll degrees of freedom at the pylon to model interface. These same configurations were adopted in the latest GVT campaign to minimize discrepancies induced by boundary conditions and to build a consistent modal reference for correlation and aeroelastic prediction [2].

2.2. Latest model modifications

Recent test campaigns showed that the support-system dynamics and the pylon–model interface details can significantly influence the low-frequency spectrum. These effects become particularly relevant when rigid-body degrees of freedom are released, as small assembly variations may alter modal spacing and correlation robustness. To improve repeatability and operational safety, two main hardware upgrades were introduced [4, 8]:

(i) **Pylon upgrade.** The original actuated pylon was replaced by a stiffer tubular steel support. This change reduces parasitic compliance and mitigates low-frequency artefacts, increasing stiffness margins for flutter testing [4].

(ii) **Pylon to model joint redesign.** The effective gimballed joint was relocated above the model centre of gravity to avoid the inverted-pendulum behaviour previously observed in the free-to-roll configuration. The redesign improves passive static stability and enables a clearer separation between stability augmentation (SAS) and Active Flutter Suppression (AFS) roles [8].

Figure 1: F-XDIA inside Galleria del vento with it latest configuration.

3. FEM model modification

3.1. Model modularization

The FEM was modified to reflect the latest pylon and pylon to model interface modifications, while preserving a modular structure suitable for iterative assembly and targeted editing. A practical strategy based on `INCLUDE` files was adopted to isolate major subsystems (e.g., pylon, wing spar) and to reduce the risk of inconsistencies when multiple upgrades are introduced across a large NASTRAN dataset. The CAD to FEM implementation was carried out in Femap/NASTRAN, enabling controlled modifications of local mesh regions affected by the new support and joint architecture, while keeping the global model compatible with the subsequent correlation workflow.

3.2. DMIG-based NeoCASS interface

NeoCASS was selected as the aeroservoelastic environment because it supports an efficient path from an FE structural description to reduced-order models suitable for flutter prediction and control-oriented state-space synthesis [1]. Since NeoCASS does not natively implement all structural modelling details available in industrial solvers, a direct matrix I/O route based on NASTRAN DMIG was employed to import externally generated high-fidelity structural portions [5, 7]. In the finalized workflow, selected subsystems (notably the solid-meshed joint region and the plate-based wing spar model) were exported as mass and stiffness matrices and integrated into the NeoCASS structural dataset, preserving their dynamic contribution while maintaining a modular global assembly.

3.3. Redesigned pylon to model attachment

The pylon to model attachment was redesigned to improve static stability and repeatability when releasing rigid-body degrees of freedom at the interface. In the previous arrangement, the effective joint location was such that the free-to-roll configuration exhibited an inverted-pendulum behaviour, introducing a strong sensitivity of the low-frequency dynamics to small assembly variations. The redesigned attachment relocates the gimballed joint above the model centre of gravity, promoting passive static stability and providing a cleaner separation between stability augmentation (SAS) and Active Flutter Suppression (AFS) objectives [4, 8].

From a modelling standpoint, the attachment region is critical because it governs the transition between: (i) clamped boundary conditions (Configuration 1) and (ii) released pitch/roll configurations (Configurations 2–4), which in turn affect the lowest part of the spectrum and may trigger mode re-ordering. Therefore, the FEM modification explicitly introduces the redesigned attachment geometry and provides a configuration-driven way to activate/release pitch and roll while keeping the remaining DOFs constrained.

The attachment CAD was processed in FEMAP to remove minor features not relevant for global dynamics (e.g., small holes, negligible fillets) and to ensure robust meshing and node-to-node connectivity across mating surfaces. The final attachment is represented as a solid-meshed substructure (first-order `CHEXA` elements) with a mesh density compatible with repeated eigensolutions during the updating loop. The solid region is then connected to the surrounding beam/plate model through shared interface nodes and/or a limited number of kinematic constraints to avoid artificial local stiffening.

To enable consistent switching among configurations without remeshing, the attachment is interfaced to the global model through a reference node and a rigid spider (`RBE2`) defined at assembly level. The rigid element constrains translations and yaw while allowing the selective release of roll and/or pitch:

- **Cfg. 1 (clamped):** all rotational DOFs constrained (equivalent fixed interface);
- **Cfg. 2 (free roll):** roll DOF released, pitch constrained;
- **Cfg. 3 (free pitch):** pitch DOF released, roll constrained;
- **Cfg. 4 (free roll + pitch):** both roll and pitch DOFs released.

This separation between *kinematic release* (through the `RBE2` DOF set) and *compliance modelling* (through `CELAS` design variables) keeps the updating problem physically interpretable and prevents the optimization from compensating boundary-condition effects via non-physical stiffness changes.

The redesigned attachment is complemented by localized equivalent compliances (implemented via `CELAS` elements) representing the net flexibility of local joint effects that are not explicitly captured by the idealized rigid constraints. These compliances are the parameters updated in the optimization loop (Section 5), while the redesigned attachment provides a more stable and repeatable baseline boundary condition across configurations.

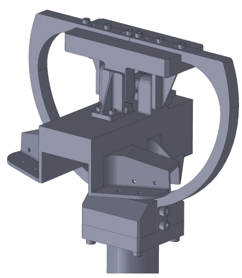

(a) Redesigned pylon to model attachment

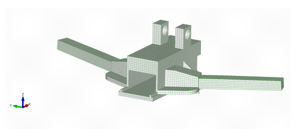

(b) FEM representation of pylon to model attachment region

Figure 2: Redesigned pylon to model attachment: (a) updated joint architecture with relocated gimbal, and (b) corresponding FEM representation enabling configuration-driven pitch/roll releases without remeshing.

4. Ground Vibration Test (GVT)

4.1. Latest campaing

A dedicated GVT campaign was performed with the model installed on the pylon according to the wind-tunnel set-up, in order to provide a consistent experimental modal database for correlation [2]. Four configurations were tested, spanning clamped and released pitch/roll boundary conditions; when pitch and/or roll were released, a rope–spring restraint limited rigid-body translations without significantly altering the elastic dynamics.

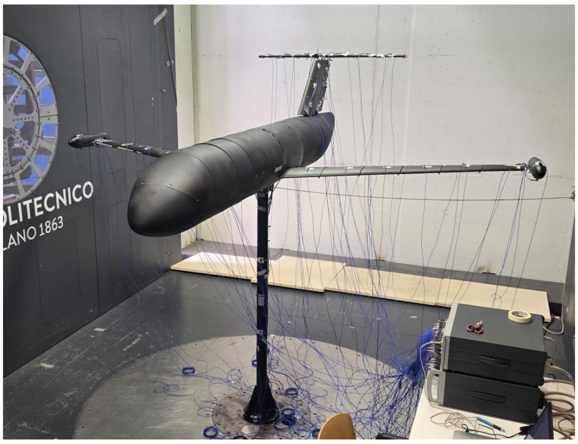

Figure 3: Ground Vibration Test set-up for the F-XDIA.

Table 1: Summary of tested configurations in the latest GVT campaign [2].

Cfg.	Constraint condition	Notes / implementation
1	Clamped to pylon	Baseline condition; reference dataset adopted for the main correlation/update activity.
2	Free roll hinge	Roll released at the pylon–model interface; rope–spring system used as translation limiter.
3	Free pitch hinge	Pitch released at the pylon–model interface; rope–spring system used as translation limiter.
4	Free roll and pitch hinges	Both roll and pitch released; rope–spring system used as translation limiter.

4.2. Instrumentation, excitation and identification

The test set-up combined multiple accelerometers distributed on the lifting surfaces and fuselage, and employed a controlled excitation strategy to ensure sufficient observability of the dominant elastic families. Modal parameters were identified through standard frequency-domain processing and validated through consistency checks (e.g., AutoMAC coherence). As expected, the lowest part of the spectrum is the most sensitive to boundary condition releases, while the primary elastic wing modes (bending and torsion) remain comparatively stable across configurations [2, 8].

5. FEM model updating

5.1. Updating strategy and metrics

The updating activity was intentionally constrained to a limited and physically interpretable parameter set, avoiding global mass/stiffness updating that may mask modelling errors through non-physical compensation. Localized interface and component-connection compliances were represented through `CELAS` elements and treated as design variables via dimensionless scaling factors applied to nominal stiffness values. For each design variable, a NeoCASS modal analysis was performed and the resulting frequencies and mode shapes were compared against the GVT targets using: (i) frequency mismatch metrics (including RMS relative error over a selected mode set), and (ii) mode-shape correlation through MAC matrices to validate modal pairing and preserve mode identity [3].

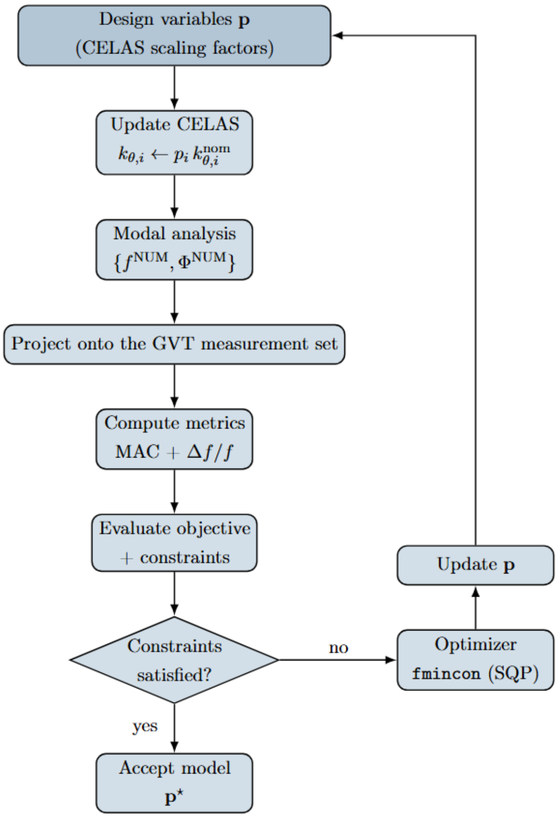

Figure 4: Block diagram of the FEM updating optimization workflow.

5.2. Design variables (selected CELAS set)

The design variable set was selected to represent the most influential interface regions identified from engineering judgement and prior campaign experience, including pylon to model compliance, ground to pylon compliance, and localized tail to fuselage and vtail to htail connections. The corresponding `CELAS` IDs used as design variables in the main optimization (Configuration 1 target dataset) are reported in Table 2.

Table 2: Set of `CELAS` elements selected as design variables for Configuration 1 correlation.

Interface / physical meaning	**ID$_x$**	**ID$_y$**	**ID$_z$**
Tail–fuselage compliance	20	21	22
Pylon–fuselage compliance	9200	9201	9202
H-tail–V-tail compliance (set A)	50301	50302	50303
H-tail–V-tail compliance (set B)	50401	50402	50403
H-tail–V-tail compliance	30	31	32
Ground–pylon compliance	101	102	103

5.3. Objective function and constraints

The design variables are defined as dimensionless scaling factors collected in the vector $\boldsymbol{s} \in R^{n_{\text{dv}}}$ and applied to the nominal stiffnesses:

$$k_i^{\text{corr}} = s_i\, k_i^{\text{ini}}, \qquad i = 1, \dots, n_{\text{dv}}. \tag{1}$$

For a given $\boldsymbol{s}$, a modal analysis provides the numerical frequencies $f_i^{\text{num}}(\boldsymbol{s})$ and mode shapes $\boldsymbol{\phi}_i^{\text{num}}(\boldsymbol{s})$, which are compared against the GVT targets f_i^{GVT} and $\boldsymbol{\phi}_i^{\text{GVT}}$ over a selected set of N modes (rigid-body modes excluded when present).

Mode pairing and MAC. Mode pairing is established by maximizing the Modal Assurance Criterion (MAC) over the selected mode set. For a candidate pair (i, j), the MAC is computed as

$$\text{MAC}_{ij}(\boldsymbol{s}) = \frac{\left| \boldsymbol{\phi}_i^{\text{GVT}\,T} \boldsymbol{\phi}_j^{\text{num}}(\boldsymbol{s}) \right|^2}{\left(\boldsymbol{\phi}_i^{\text{GVT}\,T} \boldsymbol{\phi}_i^{\text{GVT}} \right) \left(\boldsymbol{\phi}_j^{\text{num}\,T}(\boldsymbol{s}) \boldsymbol{\phi}_j^{\text{num}}(\boldsymbol{s}) \right)}. \tag{2}$$

After pairing, each experimental mode i is associated to one numerical mode $\pi(i)$.

Objective function. The objective combines frequency agreement and mode-shape correlation:

$$\min_{\boldsymbol{s}} \; J(\boldsymbol{s}) = w_f\, J_f(\boldsymbol{s}) + w_{\text{MAC}}\, J_{\text{MAC}}(\boldsymbol{s}), \tag{3}$$

where

$$J_f(\boldsymbol{s}) = \sqrt{\frac{1}{N} \sum_{i=1}^{N} \left(\frac{f_{\pi(i)}^{\text{num}}(\boldsymbol{s}) - f_i^{\text{GVT}}}{f_i^{\text{GVT}}} \right)^2}, \tag{4}$$

$$J_{\text{MAC}}(\boldsymbol{s}) = \frac{1}{N} \sum_{i=1}^{N} \left(1 - \text{MAC}_{i,\pi(i)}(\boldsymbol{s})\right), \tag{5}$$

The weights w_f, w_{MAC} are selected to balance the contribution of frequency and mode-shape terms within the optimization loop as 0.5 .

Constraints. The optimization is solved under bound constraints enforcing positive ranges:

$$0.5 \le s_i \le 2, \qquad i = 1, \dots, n_{\text{dv}}. \tag{6}$$

$$
\begin{aligned}
\min_{\mathbf{p}} \quad & J(\mathbf{p}) = 0.5\, J_{\mathrm{MAC}}(\mathbf{p}) + 0.5\, J_f(\mathbf{p}) \\
\text{s.t.} \quad & 0.5 \le p_i \le 2, \qquad i = 1, \dots, 18, \\
& \left| \frac{f_k^{\mathrm{NUM}}(\mathbf{p}) - f_k^{\mathrm{GVT}}}{f_k^{\mathrm{GVT}}} \right| \le 0.05, \qquad k = 1, \dots, 15, \\
& \mathrm{MAC}_{kk}(\mathbf{p}) \ge 0.80, \qquad k = 1, \dots, 15, \\
& p_{50301} = p_{50401}, \\
& p_{50302} = p_{50402}, \\
& p_{50303} = p_{50403}.
\end{aligned}
$$

5.4. Optimization outcome: stiffness changes

Table 3 reports the nominal and correlated stiffness values for the optimized `CELAS` set, together with scaling factors and variations. The update shows that some connections require large effective changes to reproduce the experimentally observed dynamic behaviour, highlighting the difficulty of modelling complex joints explicitly in a global FEM and motivating an equivalent-compliance representation.

Table 3: Design variables before and after the optimization process (Configuration 1 tuning).

ID	Ini.	Corr.	Scale	Δ[%]
20	2000	752 472	376.23	37 523.60
21	6100	5854	0.96	−4.03
22	1500	1097	0.73	−26.87
30	20 000	1191	0.06	−94.05
31	20 000	1 804 141	90.21	8920.71
32	20 000	1 591 615	79.58	7858.08
101	700 000	811 277	1.16	15.90
102	800 000	782 115	0.98	−2.24
103	20 000	593 061	29.65	2865.31
9200	35 000	20 140	0.58	−42.46
9201	9560	7576	0.79	−20.75
9202	22 500	72 248	3.21	221.70
50301–50401	20 000	8544	0.43	−57.28
50302–50402	20 190	39 050	1.94	93.41
50303–50403	20 000	10 996	0.55	−45.02

5.5. Correlation results across configurations (Cfg. 1–Cfg. 4)

The parameter set was tuned on Configuration 1 (clamped to pylon). The resulting correlated model was then assessed on the remaining configurations without any additional retuning: only the boundary-condition change associated with each configuration was applied at assembly level. When rigid-body freedoms are released, the lowest part of the spectrum becomes more sensitive to pylon to model joint dynamics and mode ordering may change more easily; therefore, rigid-body modes are excluded from the quantitative frequency assessment in the released configurations.

Table 4: Frequency-correlation metrics across configurations (initial vs. correlated-on-Cfg. 1).

Cfg.	BC	Modes	$\mathrm{RMS}_{\mathrm{ini}}$ [%]	$\mathrm{RMS}_{\mathrm{corr}}$ [%]
1	C	15	6.64	6.95
2	R	14	7.73	5.78
3	P	14	11.84	15.13
4	RP	13	15.87	20.18

Note: BC codes: C = clamped, R = free roll, P = free pitch, RP = free roll + pitch. In released configurations, rigid-body modes are excluded from the count (Cfg. 2: roll; Cfg. 3: pitch; Cfg. 4: roll+pitch).

Configuration 1 (clamped): post-updating behaviour. On the updating configuration, the overall RMS frequency error remains of the same order, while the MAC matrix becomes more diagonal-dominant. This indicates a more consistent numerical/experimental pairing for most modes, with residual non-ideal correlation mainly associated with closely spaced families and modes with similar shapes.

Configuration 2 (free roll): transferability improves. Since the first identified mode is rigid body roll, it is excluded and the comparison is performed over 14 modes. The correlation tuned on Configuration 1 remains transferable: the RMS relative frequency error reduces from 7.73% (initial) to 5.78% (correlated), suggesting that the updated interface stiffness representation is not strictly configuration-specific. MAC matrices confirm clear pairing for the main elastic families, with limited off-diagonal peaks attributable to mode re-ordering and increased rigid-body content.

Configuration 3 (free pitch): increased sensitivity and modal mixing. Since the first identified mode is rigid body pitch, it is excluded and the comparison is performed over 14 modes. When the pitch degree of freedom is released, the low-frequency dynamics become more governed by hinge/support behaviour and by the coupling between rigid-body and elastic content. Accordingly, the RMS relative frequency error increases from 11.84% (initial) to

15.13% (correlated-on-Cfg. 1), and MAC matrices show increased mixing. Despite this, the correlated model remains suitable for aeroelastic prediction (Section **??**) because the instability mechanism is dominated by the coupled bending–torsion family that is well observed and correctly represented.

Configuration 4 (free roll + pitch): most demanding case. In Configuration 4 the first two identified modes correspond to roll and pitch rigid body motions; therefore, they are excluded and the comparison is performed over 13 modes. This configuration is the most challenging for transferability: the RMS relative error is 15.87% for the initial model and increases to 20.18% when applying the Configuration 1-based correlation. MAC matrices reveal reduced diagonal dominance and stronger off-diagonal peaks, consistent with increased modal mixing and mode swapping among closely spaced modes. These results motivate configuration-specific extensions of the updating strategy when strict structural correlation is required under multiple released degrees of freedom.

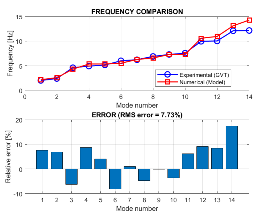

(a) Cfg. 2: freq. ini vs. GVT (RMS = 7.73%).

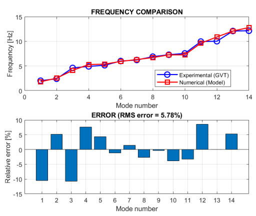

(b) Cfg. 2: freq. corr vs. GVT (RMS = 5.78%).

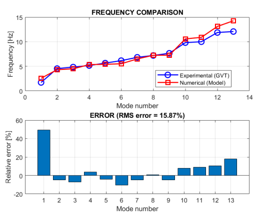

(c) Cfg. 4: freq. ini vs. GVT (RMS = 15.87%).

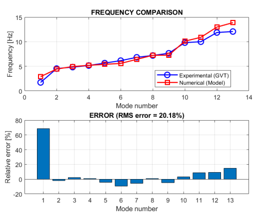

(d) Cfg. 4: freq. corr vs. GVT (RMS = 20.18%).

Figure 5: Frequency correlation transferability for released configurations: Configuration 2 (top row) and Configuration 4 (bottom row).

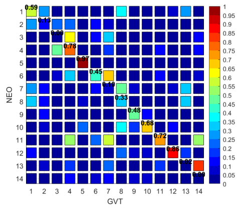

(a) Cfg. 2: MAC ini vs. GVT.

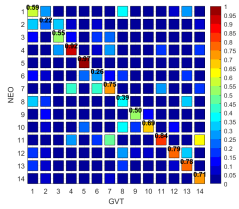

(b) Cfg. 2: MAC corr vs. GVT.

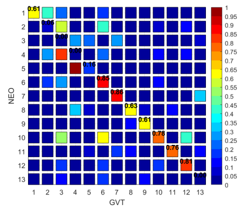

(c) Cfg. 4: MAC ini vs. GVT.

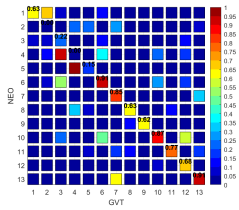

(d) Cfg. 4: MAC corr vs. GVT.

Figure 6: MAC matrices highlighting increased modal mixing when multiple rigid-body releases are introduced (Configuration 4) compared to the single-release case (Configuration 2).

6. Flutter analysis

6.1. Flutter criterion

Flutter prediction was performed in the NeoCASS framework by solving the coupled aeroelastic eigenvalue problem over an airspeed sweep. For each eigenvalue $\lambda(V) = \sigma(V) + i\omega_d(V)$, the damping ratio is computed as

$$\xi(V) = -\frac{\Re(\lambda)}{|\lambda|}, \tag{7}$$

and the commonly used aeroelastic damping parameter is $g(V) = 2\xi(V)$. Flutter onset is detected when the damping crosses zero (equivalently $\sigma = 0$ or $\xi = 0$), marking the transition from stable to unstable response.

6.2. Summary flutter onsets across configurations

Table 5 summarizes the predicted flutter onsets for the four configurations. Across all configurations, the *first* instability is consistently associated with a *symmetric wing bending–torsion* coupling. A representative mode-shape visualization is reported in Figure 7. The *second* instability typically involves a different coupling pattern, with antisymmetric bending and torsion and tail bending.

Table 5: Predicted flutter onsets across configurations.

Cfg.	BC	$V_{F,1}$ [m/s]	$V_{F,2}$ [m/s]
1	clamped	37.4	49.7
2	free roll	36.2	50.1
3	free pitch	40.8	47.1
4	free roll + pitch	39.2	49.2

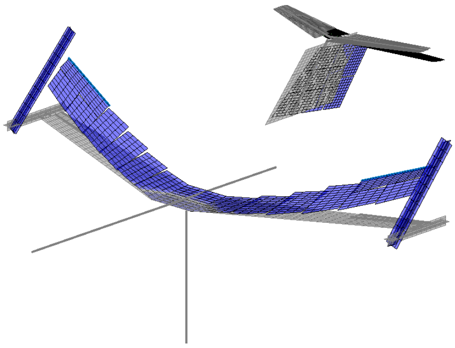

Figure 7: First flutter mode shape (common trend across configurations): symmetric wing bending and wing torsion.

6.3. Configuration 1 (clamped to pylon)

For the clamped configuration, the predicted instability mechanism of the first flutter onset is consistent with a symmetric wing bending–torsion coupling. Figures 8–9 report the stability trends.

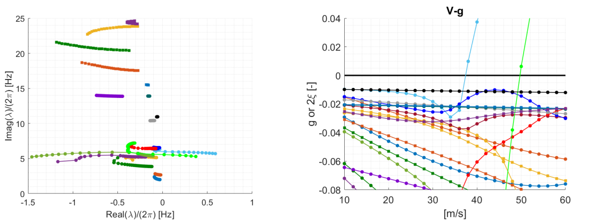

(a) Root-locus evolution (Cfg. 1). (b) $V-g$ with flutter crossings (Cfg. 1).

Figure 8: Configuration 1: stability trends from the NeoCASS flutter solution.

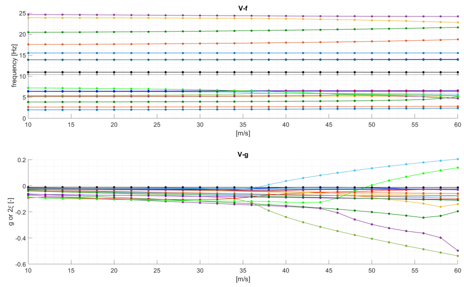

Figure 9: Configuration 1: $V-f$ and $V-g$ diagrams (NeoCASS).

6.4. Configuration 2 (free roll hinge)

When the roll degree of freedom is released, the low-frequency dynamics are more sensitive to support/interface modelling; nevertheless, the first flutter mechanism remains dominated by the symmetric wing bending–torsion coupling. Figures 10–11 summarize the results.

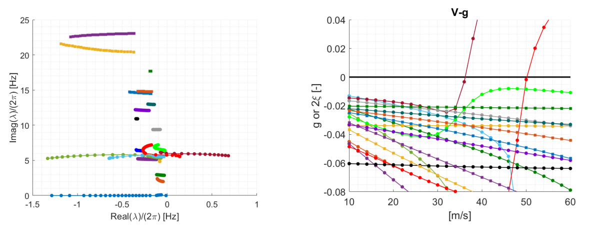

(a) Root-locus evolution (Cfg. 2). (b) $V-g$ with flutter crossings (Cfg. 2).

Figure 10: Configuration 2: stability trends from the NeoCASS flutter solution.

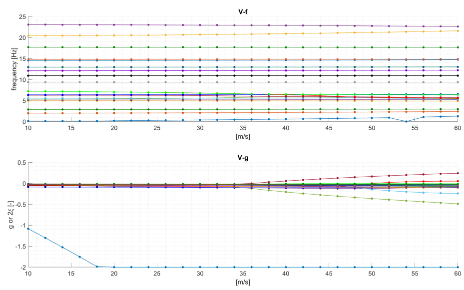

Figure 11: Configuration 2: $V-f$ and $V-g$ diagrams (NeoCASS).

6.5. Configuration 3 (free pitch hinge)

For Configuration 3, two distinct instabilities are identified: the first flutter occurs at $V_{F,1} = 40.8$ m/s, followed by a second flutter mechanism at $V_{F,2} = 47.1$ m/s. The first flutter mode is characterized by a symmetric wing bending–torsion coupling, consistently with the trend observed across configurations.

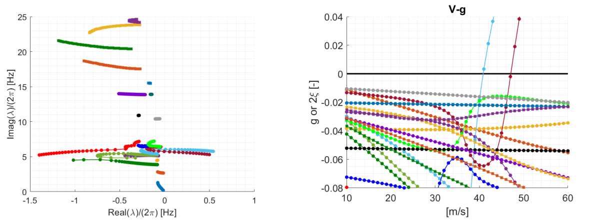

(a) Root-locus evolution (Cfg. 3).

(b) $V-g$ with flutter crossings (Cfg. 3).

Figure 12: Configuration 3: stability trends from the NeoCASS flutter solution. Flutter onsets detected at $V_{F,1} = 40.8$ m/s and $V_{F,2} = 47.1$ m/s.

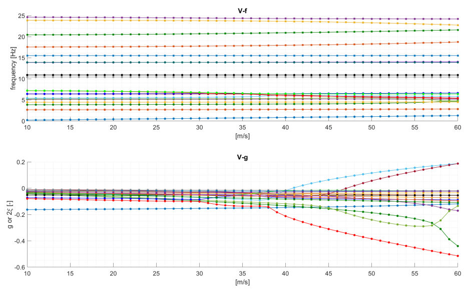

Figure 13: Configuration 3: $V-f$ and $V-g$ diagrams (NeoCASS). Two instabilities are detected at $V_{F,1} = 40.8$ m/s and $V_{F,2} = 47.1$ m/s.

6.6. Configuration 4 (free roll and pitch hinges)

Configuration 4 is the most demanding boundary condition, as multiple rigid-body releases increase modal interaction at low frequencies. Despite the increased sensitivity, the first flutter mechanism remains associated with the symmetric wing bending–torsion coupling. Figures **??**–15 provide the predicted stability trends.

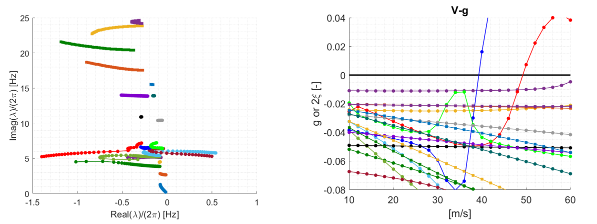

(a) Root-locus evolution (Cfg. 4).

(b) $V-g$ with flutter crossings (Cfg. 4).

Figure 14: Configuration 4: stability trends from the NeoCASS flutter solution.

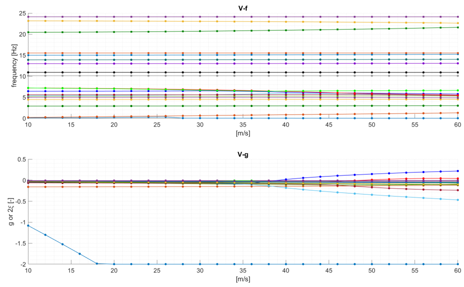

Figure 15: Configuration 4: $V-f$ and $V-g$ diagrams (NeoCASS).

7. Comparison with wind tunnel data (Configuration 3)

7.1. Experimental benchmark

The wind-tunnel benchmark is based on the sum of measured Frequency Response Functions (FRFs) between the aileron command (input) and wing-tip accelerometers (outputs). Tracking FRF peaks across the velocity sweep enables a direct interpretation of the dominant aeroelastic resonances. Two prominent peaks remain identifiable and are associated with wing bending and wing torsion. Approaching flutter, the peaks move closer and progressively merge: the peak coalescence around $V \approx 40.2$ m/s provides a physically interpretable marker for the onset of the instability [6, 9].

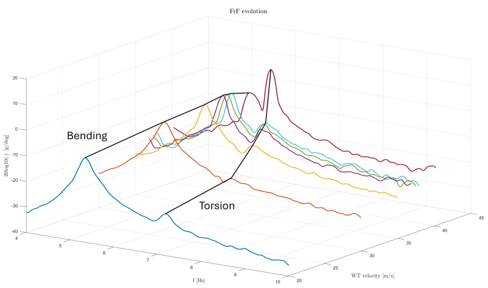

Figure 16: Experimental FRF evolution with airspeed for Configuration 3, showing bending–torsion interaction and peak coalescence approaching $V \approx 40.2$ m/s [9].

7.2. Flutter speed and frequency agreement

Table 6 summarizes the discrepancy between measured and predicted flutter quantities for different modelling approaches. The initial model underpredicts the flutter speed, while the model correlated on Configuration 1 provides a close match of the experimental marker (error $\approx$ 1.5%). A Configuration 3-specific update (performed using the same methodology on the corresponding GVT dataset) provides an alternative correlated reference, also reported for completeness.

Table 6: Comparison of flutter speed and flutter frequency for different modelling approaches.

	WT	Ini.	Corr.	Corr. C3
V_f [m/s]	40.20	36.10	40.80	39.00
ε_V [%]	—	10.20	1.50	2.98
f_{fl} [Hz]	6.20	6.04	6.04	6.15
ε_f [%]	—	2.58	2.58	0.80

7.3. $V-f$ and $V-g$ trend comparison

Beyond the scalar flutter marker, the comparison was extended by overlaying experimentally identified modal frequencies and damping estimates onto the numerical flutter branches. The $V-f$ comparison provides a visually guided association between FRF peaks and numerical eigen-branches approaching each other near flutter; overall, the correlated model reproduces the dominant frequency migration with good accuracy (order of a few percent over the investigated range).
In contrast, the $V-g$ comparison is less consistent: experimentally identified damping ratios show significant scatter and do not follow a robust trend that can be directly matched by the numerical model. This is not unexpected, because damping estimation from FRF-based identification (especially close to modal interaction and with limited signal-to-noise ratio) is typically less reliable than frequency estimation. In this work, the update targeted only localized stiffness/compliance terms and did not attempt a dedicated damping update; therefore, the primary expected improvements are in modal spacing and mode-shape consistency, rather than in absolute damping levels.

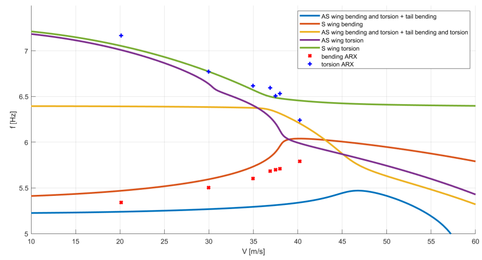

Figure 17: $V-f$ comparison for Configuration 3: experimental ARX-identified modal frequencies (markers) overlaid on numerical flutter branches (lines).

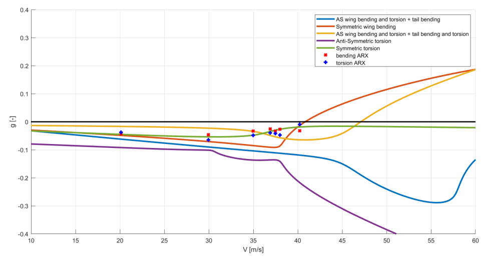

Figure 18: $V-g$ comparison for Configuration 3: experimental ARX-identified damping estimates (markers) overlaid on numerical stability trends (lines).

8. Conclusions

The thesis delivered an updated structural representation of the F-XDIA wind-tunnel model consistent with the latest hardware modifications of the support and pylon to model interface, and established a practical correlation/update workflow grounded on GVT data. A constrained optimization strategy was developed to update a limited set of localized interface compliances represented by `CELAS` elements, improving modal pairing robustness as measured by MAC while maintaining comparable frequency agreement on the target configuration. Transfer to released boundary conditions (free pitch) highlighted the increased sensitivity of low-frequency dynamics to hinge/support behaviour, motivating configuration-specific extensions of the update when strict structural correlation is required.

Despite these limitations, the correlated model provided a credible aeroelastic prediction for the wind-tunnel benchmark of Configuration 3: the first predicted flutter onset at $V_{F,1} = 40.8$ m/s matches the experimental FRF peak-coalescence marker at $V \approx 40.2$ m/s within about 1.5%, and the instability mechanism is consistently interpreted as a wing bending–torsion coupling. Future work aimed at further improving generalization across configurations and matching $V\text{–}g$ trends would require an expanded updating strategy including additional structural parameters beyond localized connection compliances, together with dedicated damping characterization.

9. Acknowledgements

The author gratefully acknowledges PhD Francesco Toffol for continuous guidance throughout the work and Prof. Sergio Ricci for supervision and support in the activity within the broader aeroservoelastic research context.

References

[1] Luca Cavagna, Sergio Ricci, and Lorenzo Travaglini. Neocass: An integrated tool for structural sizing, aeroelastic analysis and mdo at conceptual design level. *Progress in Aerospace Sciences*, 47(8):621–635, 2011.

[2] Paolo Cordisco and Matteo Terraneo. Ground vibration test (gvt) of complete version 4 of x-dia wind tunnel model. Technical Report 007/2025, Vicoter (Politecnico di Milano), August 2025. Report date: 22 August 2025.

[3] Domenico Di Leone, Francesco Lo Balbo, Alessandro De Gaspari, and Sergio Ricci. Model updating and aeroelastic correlation of scaled wind tunnel model for active flutter suppression test. *Aerospace*, 8(11), 2021.

[4] Nicola Fonzi, Sergio Ricci, and Eli Livne. Wind tunnel tests of an aeroelastic model with multiple control surface freeplay nonlinearities. In *AIAA SciTech 2024 Forum*. American Institute of Aeronautics and Astronautics, 2024. AIAA Paper 2024-1269, Orlando, FL, USA.

[5] Hexagon AB and/or its subsidiaries. *MSC Nastran 2024.2 Quick Reference Guide*, November 2024. Release: MSC Nastran 2024.2.

[6] Sergio Ricci, Francesco Toffol, Alessandro De Gaspari, Luca Marchetti, Federico Fonte, Luca Riccobene, Paolo Mantegazza, John Berg, Eli Livne, and Kristi Morgansen. Wind tunnel system for active flutter suppression research: Overview and insights. *AIAA Journal*, 60(12):6692–6714, 2022.

[7] Francesco Toffol, Nicola Fonzi, Giampiero Bindolino, Sergio Ricci, John Berg, and Eli Livne. Experimental identification and control of flutter beyond the first flutter mechanism. In *AIAA SciTech 2024 Forum*. American Institute of Aeronautics and Astronautics, 2024. AIAA Paper 2024-1268.

[8] Francesco Toffol, Matteo Paolini, Luca Riccobene, Donato Grassi, Sergio Ricci, John Berg, and Eli Livne. Study on interaction between a stability augmentation system and an active flutter suppression controller. In *AIAA SciTech 2025 Forum*. American Institute of Aeronautics and Astronautics, 2025. AIAA Paper 2025-1853.

[9] Francesco Toffol, Elena Roncolini, Sergio Ricci, and Eli Livne. Freeplay and preload effects on the aeroelastic behavior of the xdia wind tunnel model: 2025 test results and insights. In *AIAA SCITECH 2026 Forum*, page 1059, 2026.